ARTICLE

Deterministic Nanopatterning of Diamond Using Electron Beams

James Bishop,[*],[†],[§] Marco Fronzi,[†],[‡],[§] Christopher Elbadawi,[†] Vikram Nikam,[†] Joshua Pritchard,[†] Johannes E. Fröch,[†] Ngoc My Hanh Duong,[†] Michael J. Ford,[†] Igor Aharonovich,[†] Charlene J. Lobo,[†] and Milos Toth[†]

†School of Mathematical and Physical Sciences, University of Technology, Sydney, P.O. Box 123, Broadway, Sydney, New South Wales 2007, Australia

‡International Research Centre for Renewable Energy, State Key Laboratory of Multiphase Flow in Power Engineering, Xi'an Jiaotong University, Xi'an 710049, Shaanxi, China

S Supporting Information

ABSTRACT: Diamond is an ideal material for a broad range of current and emerging applications in tribology, quantum photonics, high-power electronics, and sensing. However, top-down processing is very challenging due to its extreme chemical and physical properties. Gas-mediated electron beam-induced etching (EBIE) has recently emerged as a minimally invasive, facile means to dry etch and pattern diamond at the nanoscale using oxidizing precursor gases such as O_2 and H_2O. Here we explain the roles of oxygen and hydrogen in the etch process and show that oxygen gives rise to rapid, isotropic etching, while the addition of hydrogen gives rise to anisotropic etching and the formation of topographic surface patterns. We identify the etch reaction pathways and show that the anisotropy is caused by preferential passivation of specific crystal planes. The anisotropy can be controlled by the partial pressure of hydrogen and by using a remote RF plasma source to radicalize the precursor gas. It can be used to manipulate the geometries of topographic surface patterns as well as nano- and microstructures fabricated by EBIE. Our findings constitute a comprehensive explanation of the anisotropic etch process and advance present understanding of electron-surface interactions.

KEYWORDS: nanofabrication, directed lithography, diamond, electron beam-induced etching, patterning, chemical rate kinetics, anisotropy
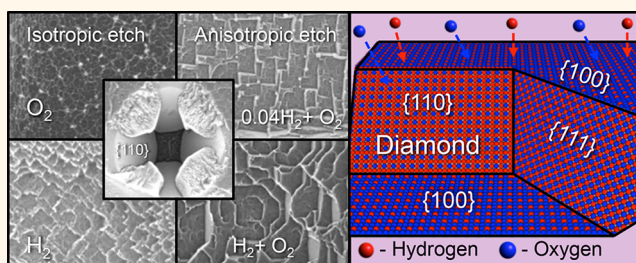
Diamond is a material of choice for many applications due to its extreme chemical stability, high thermal conductivity, and excellent acoustic and optical properties. To this extent, diamond has been explored in the context of emerging quantum photonic technologies,[1−3] nonlinear optics,[4,5] microelectromechanical systems (MEMS),[6] acoustic devices,[7] and electrochemistry.[8] It also holds promise for improving the performance of more conventional electronic devices.[9−11] However, due to its high chemical stability, it remains challenging to etch and nanostructure diamond in a minimally invasive manner that does not compromise the functionality of device-grade optoelectronic materials.[12−16]

For many of those applications, controlling the diamond surface is of paramount importance. For example, inducing controlled patterning to expedite neuron growth on diamond surfaces has been a long-standing goal in exploiting diamond in biosensing applications.[17] For photonic applications, enhancing light extraction by ameliorating the diamond surface *via* direct patterning of cones can also be advantageous.[18,19] Exposing particular surfaces (*e.g.* {111} over {100} planes) can be a viable method to enhance incorporation of color centers.[20] Finally, emerging applications of diamond in electrochemistry and catalysis are only in their infancy,[21,22] and morphology control by direct surface patterning can be highly beneficial to improve final device performance.

Electron beam-induced etching (EBIE)[23−26] has recently emerged as a versatile technique that can be used to etch diamond with no damage detected by Raman and photoluminescence spectroscopy.[19] The technique is capable of single step, beam-directed chemical etching of a broad range of materials[27−30] with high spatial resolution (∼10 nm).[31,32] Etching proceeds through material volatilization pathways driven by electron irradiation in the presence of a precursor

gas and is typically performed using a scanning electron microscope (SEM). Diamond is usually etched using O_2 or H_2O precursor gases, and most studies of EBIE report etching that is isotropic.[33−35] However, we recently demonstrated that H_2O EBIE of single crystal diamond is anisotropic and, as a result, yields nanostructured topographic surface patterns.[36] In the same study, it was shown that the pattern geometry is governed by the symmetry of the crystal lattice and the chemical species of the precursor molecules. However, the origin of the anisotropy remains a matter of debate, and the roles of different gas molecules and molecule fragments at the diamond surface are unknown.

In the present study we use a combined experimental and density functional theory (DFT) approach to explain the roles of hydrogen and oxygen in EBIE of diamond. We show that the use of O_2 as the precursor gas gives rise to high-rate, isotropic etching of single crystal diamond, while the addition of H_2 reduces the etch rate and makes it anisotropic due to preferential passivation of specific crystal planes (i.e., hydrogen alters the etch selectivity of certain crystal planes over others). We elucidate the diamond volatilization mechanism and show that the anisotropy and the geometries of the resulting surface structures can be controlled over a broad range of length scales by the partial pressure of hydrogen and by using a remote RF plasma source to radicalize the precursor gas. The work also shows that residual H_2O contaminants play a critical role in etch rate anisotropy and that these undesired side-effects can be suppressed using a remote RF plasma source. Our results increase the present understanding of electron-surface inter-actions and are important for the design and control of electron stimulated nanofabrication processes.

RESULTS AND DISCUSSION

A schematic depicting the experimental setup used for EBIE is shown in Figure 1. In order to determine the roles of hydrogen and oxygen species in etching of diamond, we performed experiments using high-purity H_2, O_2, H_2O, and mixtures of these gases as the etch precursors. It must first be noted that highly controlled environments are essential for reproducible EBIE. Organic contaminants must be removed from samples
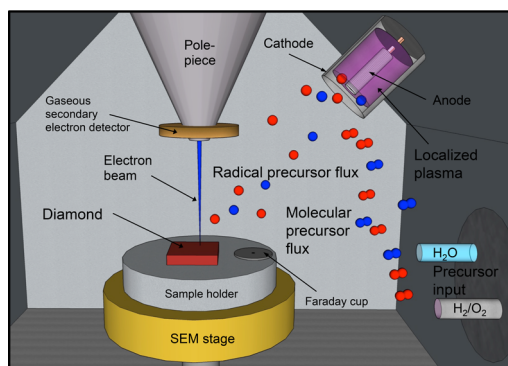

Figure 1. Schematic of the experimental apparatus used for EBIE. The field emission gun SEM is outfitted for variable-pressure operation, and an external gas delivery system enables precise metering and delivery of the gases O_2, H_2, Ar, N_2, and H_2O. H_2O is delivered via a dedicated line to avoid contamination of other gases. An in situ RF remote plasma generator serves a dual purpose. It is used prior to EBIE with O_2 gas to reduce the concentration of residual organic and water contaminants and during EBIE to radicalize precursor gases and increase their reactivity.

prior to EBIE, and the necessary sample preparation procedures are detailed in the Methods section and Supporting Information (SI). It must also be noted that residual H_2O is abundant in the high-vacuum systems normally used for EBIE, and it gives rise to electron-induced oxidation and etching of carbonaceous materials.[37−39] Active suppression of residual H_2O was found to be the second necessary prerequisite for the present study, and we discovered that the use of a low-power RF remote plasma generator can not only eliminate the effects of organic contaminants[40,41] but also those of residual water. It can therefore enable robust electron stimulated processing of surfaces, as is detailed below.

Figure 2 shows a set of etch pits fabricated by EBIE in {100}-oriented, B-doped, CVD grown, type 2a single crystal (SC) diamond using H_2 and O_2 precursor gases. All results presented in this work were obtained at room temperature (RT), except for Figure 1 of the SI. Each etch pit was made by scanning the electron beam in a rectangular raster pattern. R_p designates the ratio of the H_2 to the O_2 partial pressure, which was varied from pure O_2 (Figure 2a) to a value of 8.6 (Figure 2g) by controlling the flow rates of the individual precursor gases. In addition, Figure 2h,i shows etch pits fabricated using pure H_2 and pure H_2O, respectively. The latter is included here for reference and shows the topographic patterns reported in our prior work on H_2O EBIE of diamond.[36]

Using pure O_2 ($R_p \approx 0$), we observe a "sponge-like" surface texture at the etch pit base (Figure 2a), and the morphological features are not aligned with crystallographic directions. The lack of pattern formation shows that O_2 EBIE gives rise to isotropic etching of diamond. As hydrogen is added to the system (increasing R_p in Figure 2), we observe surface patterns comprised of features aligned with crystallographic directions. This is indicative of anisotropic etching caused by variations in the etch rate (i.e., selectivity) of different crystal planes. The etch frames are aligned with the edge of the diamond prior to EBIE[36] such that all etch pit sidewalls are approximately parallel to ⟨100⟩ directions. At low R_p values (corresponding to small amounts of H_2), we observe square and rectangular patterns (Figure 2b,c) which evolve toward octagonal patterns at elevated R_p values (Figure 2d−g). In pure H_2 ($R_p \rightarrow \infty$), the pattern edges are aligned at 45° with respect to ⟨100⟩ crystal directions (Figure 2h).

Electron irradiation of diamond in the presence of the inert gases N_2 and Ar did not give rise to etching (see SI Figure 3), and we attribute prior reports of EBIE by these gases[42,43] to the effects of residual H_2O demonstrated previously.[37] While pure H_2 gives rise to etching of diamond, the etch rate is very low compared to that of O_2 EBIE (under equivalent conditions), indicating that the etch pathway is significantly less efficient. We obtained an etch rate of 0.32 μm^3/min for O_2 and 0.06 μm^3/min for H_2 (see SI Figure 4), under our experimental conditions (detailed in Methods). Using H_2O as precursor (Figure 2i), octagonal patterns form similar to those fabricated using a mixture of H_2 and O_2 at R_p = 1.67. However, the etch rate is significantly lower with H_2O than with O_2 as can be clearly seen in Figure 2 and SI Figure 4 (the same beam conditions and etch times were used for all pits, and all single precursor etch pits were fabricated using the same total pressure).

The geometries of the observed topographic patterns that form are dictated by the slowest etching crystal plane(s).[36] During ansiotropic chemical etching, material is removed primarily along direction(s) normal to the fast etching planes.
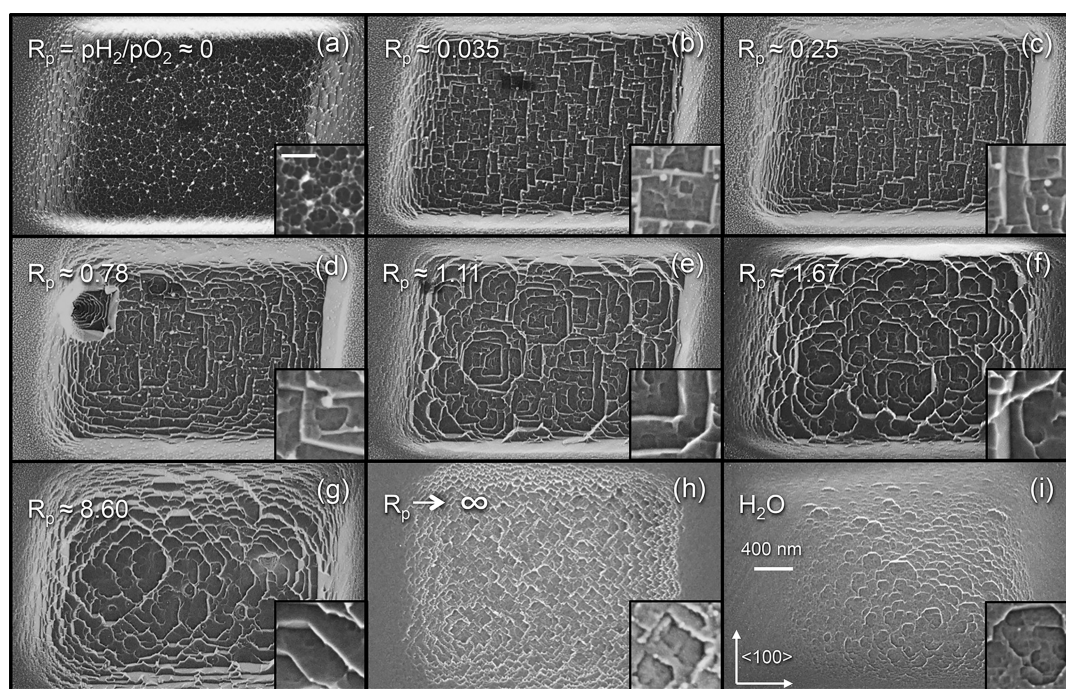
Figure 2. EBIE of {100} plane SC diamond using different ratios of H_2 and O_2 precursor gases. A remote plasma was used during EBIE for precursor radicalization and residual water reduction. The partial pressure ratio of hydrogen to oxygen (R_p) used for each etch is indicated. Insets (all at the same scale, scale bar = 100 nm) show close-ups of key surface morphologies. We observe a "sponge-like" texture and lack of patterns with pure O_2 indicating an isotropic etch (a). As R_p is increased, we see rectangular {110} basis patterns (b−c) and increasing contributions from {111} planes (d−g), resulting in octagonal patterns. Pure H_2 results in {111} basis patterns (h). EBIE with H_2O also gives rise to octagonal patterns (i). Etch times and conditions were equal for all pits. The pit depths are 894 (a), 460 (b), 530 (c), 552 (d), 450 (e), 451 (f), 545 (g), 157 (h), and 258 nm (i), respectively. The etch rate with H_2O or H_2 is lower than with O_2 or $O_2 + H_2$. The etch pit sidewalls are aligned with the substrate edges and therefore ⟨100⟩ crystal directions which are indicated in (i) and apply to all images. Edges aligned with pit sidewalls are formed by {110} planes and those at 45° by {111} planes. All main images are at the same scale indicated by the scale bar in (i).

As a result, etch fronts propagate preferentially along these fast etching directions[44,45] and expose slow etching planes which then act as a barrier to inhibit etch front propagation. Large regular features with smooth faces composed entirely of the slowest etching plane are expected if etching is continued for a sufficient amount of time.[46]

A crystallographic analysis of the patterns formed in the etch pits of Figure 2 is presented in Figure 3. Using pure O_2, no patterns are observed and etching is isotropic, while the addition of hydrogen gives rise to the formation of planes of the {110} family. We refer to these patterns as {110} basis. As R_p is increased, planes of the {111} family are partially formed with edges aligned with ⟨110⟩ directions (45° to ⟨100⟩ directions). This results in the octagonal patterns observed at higher R_p. We refer to these patterns as '{110} + {111}' basis. It must be noted that while smooth {110} planes do form, {111} planes always appear rough and partly etched. As R_p is increased further toward infinity, {111} planes contribute increasingly to the patterns. Using pure H_2, the majority of edges in the patterns are aligned with ⟨110⟩ directions and formed by {111} planes. We refer to these patterns as {111} basis. However, even with pure H_2, large smooth {111} planes do not form.

Role of a Remote Plasma in EBIE of Diamond. In this section we elucidate the roles of a remote plasma on EBIE performed using O_2, H_2, and H_2O precursor gases and on residual H_2O contaminants. The patterns discussed up to this point were fabricated by EBIE performed in the presence of a remote plasma which serves to radicalize the precursor gas, but

does not give rise to etching in the absence of the electron beam (see SI, section 1.5).

If the plasma is used to precondition the SEM chamber and the sample, but extinguished during EBIE, R_p-dependent pattern evolution is observed, but the effects of hydrogen are less pronounced as is illustrated by Figure 4. For pure oxygen ($R_p \approx 0$, Figure 4a), we observe the "sponge-like" morphology that is characteristic of isotropic O_2 etching under anhydrous conditions. However, the addition of H_2 has a lesser effect on the surface texture than when the precursor gas mixture is radicalized by a plasma. Specifically, a "sponge-like" morphology is observed even when $R_p \approx 0.26$ (Figure 4b), which is a condition at which {110} basis patterns are observed in the presence of a remote plasma (Figure 2b).

At higher hydrogen partial pressures, {110} basis patterns do occur even in the absence of a plasma, but we observe no {111} contributions to the patterns even with pure H_2 (compare Figure 2f and 2h). These results confirm that the plasma enhances the effects of hydrogen on pattern formation, which we attribute to the generation of highly reactive hydrogen radicals in the precursor gas. Conversely, when H_2O is used as the precursor gas, the patterns appear to be unaffected by the plasma (see Figure 2i and Figure 4g), as is the case for pure O_2 (see Figure 2a and Figure 4a). This is attributed to the higher reactivity and surface coverages of these gases which enhanced their efficacy as precursors for electron-stimulated surface reactions.

A reference electron exposure was performed in high vacuum using the same electron beam parameters and exposure time in
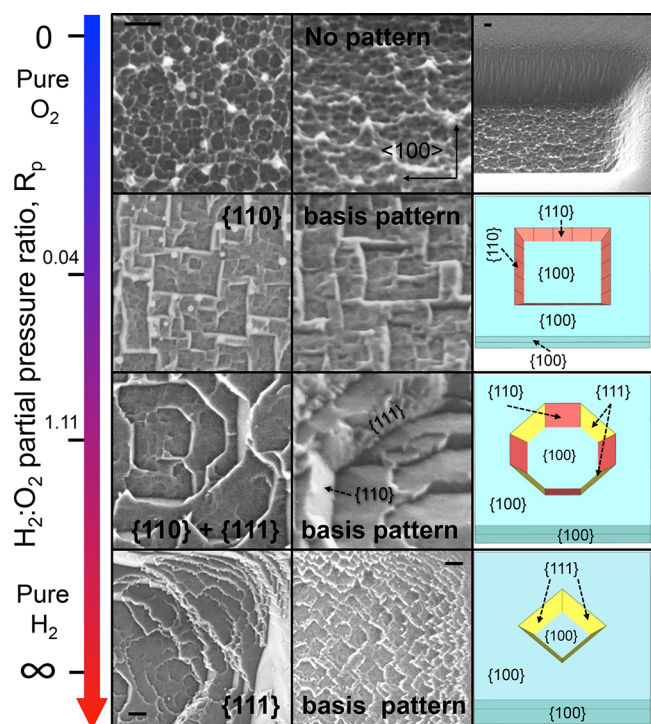
Figure 3. High-magnification SEM images of the topographical patterns formed using different ratios of H_2:O_2 (R_p) for EBIE of {100} plane diamond. Idealized geometrical figures are shown at right to aid visualization of features which comprise the patterns. With pure O_2 (top row), we obtain isotropic etching and no patterns. {110} planes form at low R_p (second row) and result in rectangular patterns. At high R_p (fourth row), {111} planes primarily dictate the patterns, forming edges aligned at 45° to ⟨100⟩ directions. At intermediate R_p (third row), we observe octagonal patterns composed of smooth {110} planes and rough {111} planes. Even with pure H_2, smooth {111} planes do not form and clearly still etch faster than {110} planes yet slower than {100} planes. Diamond-shaped features are formed, yet the geometrical ideal of an etch pit composed entirely of {111} planes is never fully realized. Images in the second column apart from the bottom image were taken at 45° tilt. Scale bars are 100 nm, and images are at the same scale as top left unless a separate scale bar is provided.

Figure 4. EBIE without plasma. (a−f) EBIE pits made with different H_2:O_2 partial pressure ratios (R_p), without the utilization of a remote plasma for precursor radicalization. Anhydrous conditions were achieved by O_2 plasma cleaning prior to EBIE, but plasma was inactive during EBIE. Adding H_2 to the system has a lesser effect on EBIE kinetics compared to when a plasma is employed. Only {110} basis patterns are observed even with $R_p \rightarrow \infty$. (g, h) A control irradiation was performed in high vacuum following EBIE with H_2 to confirm that residual water levels remained negligible throughout. High-magnification images reveal "proto-patterns" similar to those observed using H_2O as the precursor gas. Patterns formed during EBIE with H_2O are unaffected by the presence or absence of plasma. All main images are at the same scale indicated by the scale bar in (h). Insets are at the same scale (scale bar = 100 nm).

order to illustrate the role of residual H_2O in the experiments. Very slow etching is observed, seen as roughening of the diamond surface (Figure 4h), consistent with etching mediated by low levels of residual H_2O. High-magnification images of the surface reveal patterns similar to those produced when H_2O is used intentionally as an etch precursor gas, albeit on a smaller scale. The high-vacuum irradiation (Figure 4h) was performed after H_2 EBIE (Figure 4f) and prior to the intentional introduction of H_2O (Figure 4g), confirming that the surface morphology generated by pure H_2 seen in Figure 4f is not an artifact of residual H_2O.

Finally, we show directly that the above effects of residual H_2O can affect O_2 EBIE and H_2 EBIE and that the effects of H_2O contaminants can be suppressed by igniting a remote plasma either before or during etching. We start with O_2, and, critically, in this experiment we did not ignite the plasma before we performed O_2 EBIE (in contrast to the experiment shown in Figure 4). The {110} basis patterns are observed during O_2 EBIE (Figure 5a), which are indicative of etch kinetics that are affected by residual H_2O (despite overnight pumping to a base
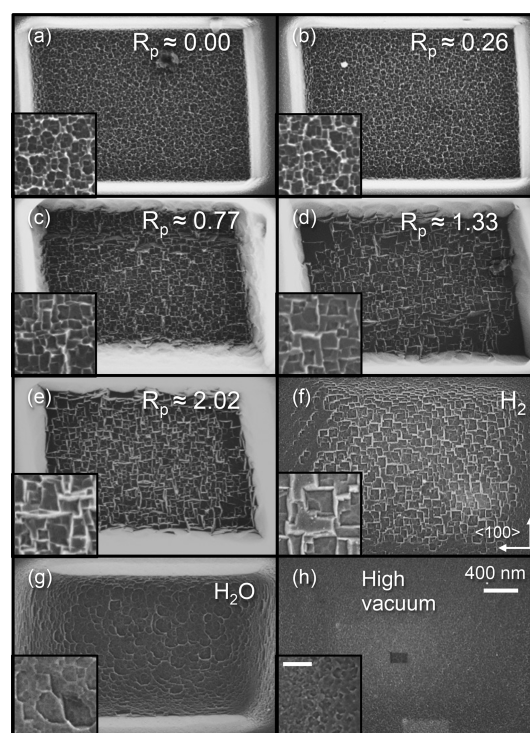
pressure of ~3.0 × 10⁻⁶ mbar prior to EBIE and the use of a cold trap on precursor gas delivery lines during etching).

We then ignited the plasma and performed the same experiment, obtaining the sponge-like texture (Figure 5b) that is characteristic of O_2-mediated EBIE under anhydrous conditions (see Figure 2a). The same etch morphology was observed for several hours after the plasma was extinguished, demonstrating that an O_2 plasma can be used prior to etching to temporarily suppress the effects of residual water.

The experiment was then repeated with H_2 precursor gas, showing that {110} and {111} basis patterns are observed in the absence (Figure 5c) and the presence (Figure 5d) of a remote plasma, respectively. The results confirm that the plasma increases the ability of H_2 to participate in EBIE. This result demonstrates unambiguously that a remote plasma can be used to activate chemically stable gases and enable their use as precursors for electron stimulated surface processing.

Role of Hydrogen in Etch Rate Anisotropy and Pattern formation. We can now interpret most of our experimental results in terms of the role of hydrogen in EBIE of diamond. In the absence of H_2, O_2-mediated EBIE of diamond is isotropic. The introduction of hydrogen stabilizes the {110}
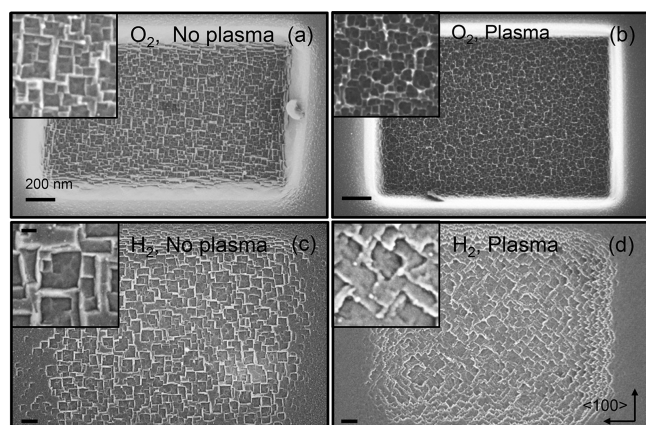
Figure 5. Effects of employing a low-power remote plasma during EBIE. (a, b) With pure O_2 as the precursor gas, the plasma eliminates the effect of residual water on EBIE. In the absence of the plasma, {110} basis patterns characteristic of O_2 EBIE affected by residual water are observed (a). With the plasma we observe the "sponge-like" texture that is characteristic of O_2 EBIE under anhydrous conditions (b). (c, d) Remote plasma radicalizes precursor gases in the chamber. This dramatically increases the reactivity of H_2 resulting in {111} and {110} basis patterns without (c) and with (d) the plasma, respectively. Scale bars in main images are 200 and 50 nm in insets. All inset images are at the same scale.

Table 1. Adsorption Energies for O, H and N Species, E_a (eV), upon the {100}, {111} and {110} Planes of Diamond[a]

Surface	Adsorption energy, E_a (eV)	
	This Work	Other Works
{100}-H	-4.72	—
{100}-H 1ML	-4.31	-4.30[47]
{100}-O(ket)	-2.83 / -6.15*	—
{100}-O(eth)	-4.17 / -7.50*	—
{100}-O 1ML (eth)	-2.30 / -5.63*	-6.21(eth)* [47]
{100}-O_2	-1.27	
{100}-OH	-3.85	-4.13[47]
{100}-N	0.02/ -4.74*	—
{111}-H	-4.37	—
{111}-H 1ML	-4.36	-4.34, -4.38[48]
{111}-O	-1.96 / -5.29*	-5.57* [49]
{111}-O 1ML	-1.66 / -4.99*	—
{111}-O_2	-1.95	—
{111}-OH	-4.38	-3.43, -4.70[48,50]
{111}-N	1.57/ -3.18*	—
{110}-H	-4.20	—
{110}-H 1ML	-4.00	-4.33[51]
{110}-O(ket)	-3.13 / -6.46*	—
{110}-O(eth)	-1.76 / -5.09*	—
{110}-O 1ML (ket)	-0.94 / -4.27*	—
{110}-O_2	-2.38	—
{110}-OH	-4.50	—
{110}-N	-0.02/ -4.77*	—

[a]1 ML denotes the adsorption energy per atom, upon a surface terminated with a monolayer of that species (highlighted). The other calculations are for a pristine, unterminated diamond surface. Energies are calculated with respect to a molecule in the gas phase, and negative values indicate attractive interactions. We also include literature values for comparison. Values sourced from literature are calculated with a range of alternative approximations and basis sets resulting in significant variation. Conclusions should be drawn only from DFT datasets calculated with the same approximations and basis sets. (Oxygen and nitrogen adsorption has also been calculated with respect to its atomic form. These values are indicated by an asterisk. The values for molecular adsorption of O_2 are reported per oxygen atom.).

plane, causing the etch rate to decrease rapidly relative to that of the {111} and {100} planes, giving rise to {110} basis patterns. As the amount or reactivity of hydrogen is increased, we eventually observe {111} contributions to the patterns (Figure 2f,g). This implies increased stabilization of the {111} plane and a decrease in the {111} etch rate and that both the {110} and {111} planes etch slower than {100} planes. The {111} features become increasingly prominent as the amount or reactivity of hydrogen is increased further, implying an additional decrease in the {111} etch rate relative to the other planes. However, we do not observe smooth {111} planes in SEM images even when pure H_2 is used as the precursor gas, indicating that the etch rate of {111} planes remains higher than that of {110} planes.

To address the question of why hydrogen modulates the etch rate in the plane-dependent manner observed in our experiments, we use DFT to calculate the adsorption energies, E_a of H and O species on diamond:

$$E_a = \frac{1}{N}[E_{Surf+Mol} - (E_{Surf} + E_{Mol})] \tag{1}$$

where $E_{Surf+Mol}$, E_{Surf}, and E_{Mol} are the energies of the molecule-surface system, the surface, and the adsorbing molecule (in the gas phase), respectively, and N is the number of molecules adsorbed per supercell.

Table 1 lists the results of E_a calculations for O, O_2, H, OH, and N species upon pristine and fully terminated (1 ML) {111}, {110}, and {100} surfaces of diamond. For adsorption of oxygen upon {110} and {100} surfaces, we consider two possible configurations: ketone and ether. O bonds to a single C atom in the ketone configuration and two atoms in the ether arrangement (see SI Figure 7). Oxygen adsorbs favorably in the ketone configuration on {111} and {110} surfaces, while ether is favorable on {100}.[52] A detailed analysis of adsorption geometries is provided in the SI. Bond distances calculated here agree well with previously reported values calculated using the DFT-GGA approximation,[49,53,54] confirming the accuracy of

our calculations. Results from simulations of both pristine and fully covered (1 ML) surfaces are presented in order to illustrate the effects of adsorbate–adsorbate interactions. However, the 1 ML results are most appropriate for direct comparison with our EBIE experiments as dangling bonds are not stable in the presence of gases which can be adsorbed.

The most important implications of these calculations are found in the comparison of O and H adsorption energies upon fully terminated surfaces. These values are highlighted in Table 1. Hydrogen adsorption can result only in bonding to a single C, the adsorption energy (E_a^H) is similar in magnitude upon all three diamond surfaces and is high relative to that of oxygen. Conversely, the oxygen adsorption energy (E_a^O) varies significantly between crystal planes. This implies that competitive adsorption of H and O will yield a different ratio of H:O coverage on each of the considered crystal planes (since the adsorbate residence time τ scales exponentially with E_a according to $\tau \propto e^{E_a/T}$, where T is temperature). The absolute value of the difference ($|E_a^H - E_a^O|$) and ratio (E_a^H/E_a^O) between the hydrogen and oxygen adsorption energies for the three planes are presented in Figure 6a. Both of these values increase in the order of {100}, {111}, {110}. As a result, we expect that during EBIE performed using a mixture of hydrogen and
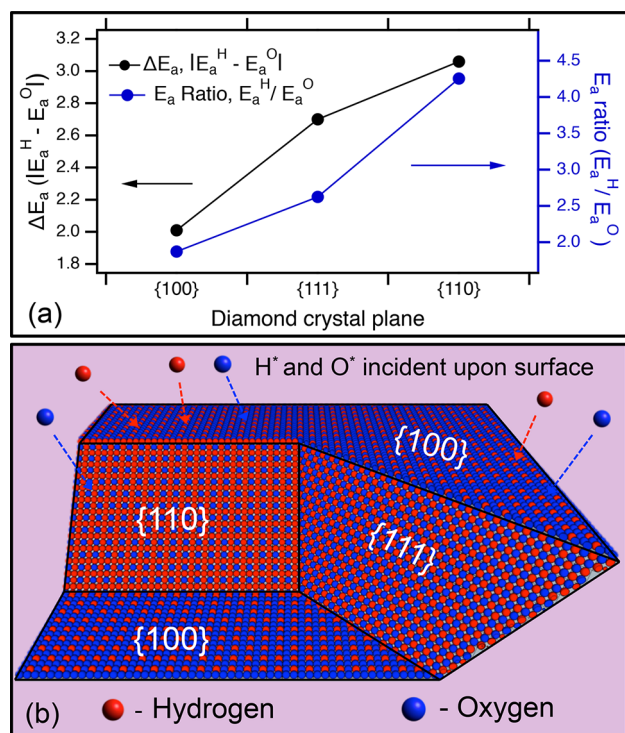
Figure 6. (a): Difference ($|E_a^H - E_a^O|$) and ratio (E_a^H/E_a^O) of full monolayer (1 ML) adsorption energies for hydrogen and oxygen on the {100}, {111} and {110} planes of diamond, calculated using DFT. The value is averaged over the number of atoms in the monolayer. (b) Conceptual schematic illustrating the implications of the calculated adsorption and desorption energies and the origin of anisotropic EBIE of SC diamond. When both H and O are present, we expect the adsorbed coverage ratio of H:O on the planes to increase in the order of {100}, {111}, {110}. The etch pathway for H terminated sites is far less efficient than O terminated sites, making the etch rate of each plane a function of the H:O surface coverage ratio.

oxygen, the coverage ratio of hydrogen to oxygen on the planes will increase in the same order. This is illustrated in Figure 6b and correlates with the anisotropic etch rates observed in EBIE experiments performed as a function of $H_2:O_2$ partial pressure. Specifically, an increase in H coverage expected from the simulations correlates with a decrease in the observed etch rate of that plane. Hence, we conclude that hydrogen acts to inhibit the oxygen-mediated etch rate, which is consistent with our observation that the H_2-mediated EBIE pathway is far less efficient (Figure 2h) than the O_2-mediated pathway (Figure 2a) and that the observed etch rate anisotropy is caused by corresponding variations in H coverage of the {100}, {111}, and {110} planes.

Etch Reaction Products. Next, we use DFT calculations to identify the most likely etch reaction product that is desorbing from diamond during oxygen-mediated EBIE. Simulations of O_2 adsorption onto pristine diamond surfaces (non-highlighted values in Table 1) indicate that, after geometry optimization, dissociative adsorption of O_2 into the C═O (ketone) or C─O─C (ether) configuration is energetically favorable over O─C─O formation (molecular adsorption, O_2) on all of the diamond surfaces considered. The high adsorption energies for ether on {100} and ketone on {110} indicate that these adsorption geometries are the most stable configurations for O on the respective planes. Following geometry optimization, no

stable ether configuration could be found upon the {111} plane (see SI Figures 7−9) and attempted molecular adsorption of O_2 upon {111} resulted in two adjacent ketone groups with approximately equal adsorption energies ({111}-O vs {111}-O_2 in Table 1). This indicates that ketone adsorption is strongly favored upon the {111} plane.[55]

Formation of stable O─C─O groups is therefore unlikely, and diamond surfaces with an O:C ratio higher than 1 are energetically unfavorable and thus unstable. CO is therefore the most likely etch product leaving the diamond surface during EBIE, since the formation of a stable etch product upon the surface is a prerequisite to electron stimulated desorption. The desorption of CO is attributed to an electron stimulated (bond scission) process since the EBIE rates of diamond are approximately independent of temperature (see ref 36 and SI Figure 1).

We note that N_2 adsorption energies in Table 1 are either positive or very low (the simulations were done using pristine diamond surfaces only since they show no significant interaction between isolated N and diamond, and the same is therefore expected for the case of monolayer N coverage). This implies that stable N-terminated sites will not form and a nitrogen-mediated etch pathway should not exist. This is consistent with our experimental observations and our claim that prior reports of the EBIE of diamond using N_2 as the precursor gas are in fact an artifact of residual H_2O.

Etch Rate Efficiency. We now turn to the question of why oxygen-mediated EBIE is more efficient than hydrogen-mediated EBIE. We used DFT to calculate desorption energies, E_d, corresponding to the desorption of a number of C-containing surface species from pristine and terminated diamond using

$$E_d = (E_{Surf-Vac} + E_{Atom}) - E_{Surf} \qquad (2)$$

where $E_{Surf-Vac}$ is the surface energy upon vacancy formation, and E_{Atom} and E_{Surf} are the energies of the surface and the desorbed species, respectively. Table 2 shows the results for a range of species on the {100}, {111}, and {110} surfaces. V_{CO} and V_{CH} indicate desorption of CO and CH, respectively, leaving a surface carbon vacancy.

The desorption energy for CO is far lower than for CH on all considered pristine diamond planes (top row of Table 2),

Table 2. Desorption Energies, E_d (eV), for {100}, {111}, and {110} Surfaces[a]

	Desorption energy, E_d (eV)		
Defect	{100}	{111}	{110}
V_{CO}	6.08	2.81	4.81
V_{CH}	11.57	10.16	10.86
H_t-V_O	2.48	2.56	1.12
H_t-V_H	4.50	4.37	3.30
O_t-V_O	2.29	1.60	0.15
O_t-V_H	4.28	4.65	2.85
H_t-V_{CO}	3.55	5.15	4.06
O_t-V_{CO}	4.33	3.85	2.72
O_t-V_{CH}	10.95	11.85	11.08
H_t-V_{CH}	10.54	11.92	11.02

[a]H_t and O_t denote hydrogen terminated and oxygen terminated surfaces respectively. Energies are calculated with respect to O, CO, and CH in the gas phase. Here, positive values indicate the energy needed to create a defect. Desorption events that give rise to etching (etch reactions) are highlighted.
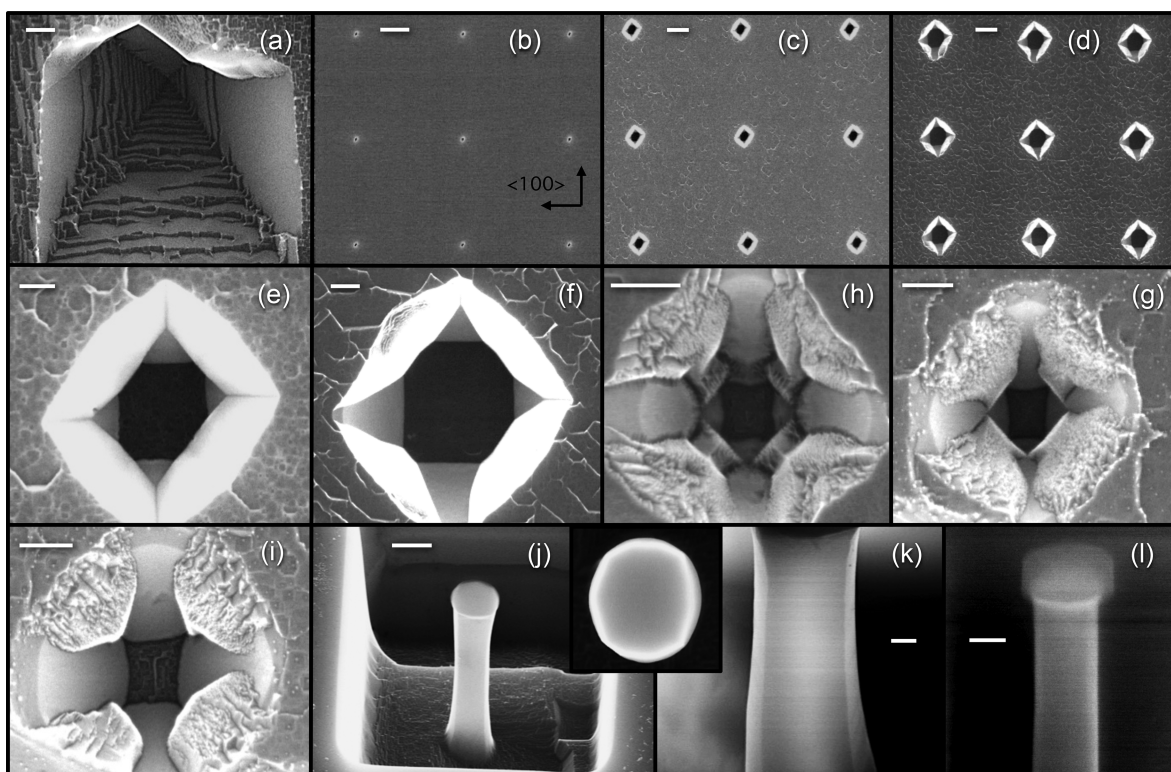
Figure 7. Structures with large crystal planes formed by anisotropic EBIE. (a) A {110} sided inverse pyramid. Such structures occasionally form in random locations during large area anisotropic etches and are attributed to subsurface defects. (b−d) Beginning with an array of approximately circular holes etched under isotropic conditions (b), inverse pyramid-like structures evolve during subsequent anisotropic EBIE of the region. (c, d) The array after 16 and 32 h of EBIE performed using a low electron flux and R_p of 2.2. (e, f) Closeups of individual structures from (c) and (d), respectively. (g−i) A similar anisotropic etch process was performed on individual circular holes similar to those in (b). (g) A structure formed from a circular hole after 40 min of anisotropic EBIE of the surrounding region. (h, i) Evolution of a separate circular hole, shown here after 30 (h) and 60 (i) min of anisotropic EBIE. The typical evolution observed involves formation of both {111} and {110} planes with the {111} planes receding and roughening, while large, smooth {110} plane sidewalls form as EBIE is continued. (j−l) Circular silica disks made with electron beam lithography can act as an electron blocking mask and allow fabrication of pillars. Anisotropic conditions yield a faceted pillar (j, k). The inset shows the silica disk atop the pillar shown in (j). The faceted pillar top can be seen through the circular outline of the mask. (l) Under isotropic conditions, a smooth cylindrical pillar is obtained. All scale bars are 200 nm except for in (b−d) and (j) which are 1 μm. The {100} crystal directions indicated in (b) apply to all images. The images in (j−l) were taken at 45, 35, and 30° tilt, respectively.

indicating a fundamental role of oxygen adatoms in weakening C−C surface bonds. Conversely, a high E_d for CH suggests surface stabilization upon hydrogen adsorption and strengthening of surface C−C bonds. E_d for desorption of CO is low relative to that of CH from all surfaces (bottom row, Table 2). The large differences between the calculated desorption energies of CO and CH correlate with the observed differences in the etch rate obtained using pure O_2 and pure H_2 precursor gases.

Finally, we note that the E_d for an etch reaction to occur (desorption of CO or CH) is higher than is required for non-etch reactions (desorption of O or H) on all surfaces. Furthermore, E_d values for non-etch reactions (entries in Table 2 that are not highlighted) are all lowest for the {110} plane. These results imply a preference for non-etch reactions over etch reactions, and this preference is greatest for the {110} plane. This correlates with the slow etch rates observed for the {110} plane during EBIE performed using a mixture of H_2 and O_2. However, we must emphasize that the energies do not translate directly to cross sections for electron stimulated desorption, and small differences between the values of E_d in Table 2 therefore do not necessarily directly correlate with variations in the EBIE rates of different crystal planes.

Fabrication of Large-Scale Structures by Anisotropic EBIE.

Anisotropic EBIE provides control over the degree of surface roughness that is needed for applications that require control over surface area and related functional properties such as wettability.[56,57] However, as we show below, the etch rate anisotropy can also be used to fabricate large-scale structures defined by the symmetry of the diamond crystal lattice and surfaces that appear very smooth in SEM and AFM images.

If EBIE is continued for extended periods under anisotropic etch conditions, inverse pyramid structures with smooth {110} plane sidewalls can form within etch pits. An example is shown in Figure 7a, and the etch pit shown in Figure 2d shows a less evolved example. We attribute their nucleation to the presence of subsurface defects and employ a two-step etch process to fabricate similar structures deterministically. An array of approximately circular holes is first made using isotropic conditions (pure O_2, Figure 7b). This is then followed by etching of the entire array under highly anisotropic conditions ($H_2 + O_2$, $R_p \approx 2.2$). Plasma is used during both steps to ensure a high degree of isotropy and anisotropy, respectively. Figure 7c,d illustrates the time-evolution of the array by images acquired at different stages during anisotropic etching. Figure 7e,f shows close-ups of individual structures from (c) and (d),

respectively. The holes initially evolve into structures with smooth {111} planes at the top and smooth {110} planes below with a rough etch pit base. As etching is continued, the {111} planes recede, and the {110} planes grow. In a similar experiment, anisotropic EBIE was performed on individual circular holes. Figure 7g–i shows representative examples of typical structures observed at different stages of anisotropic etching. Both {111} and {110} planes initially form, with the {111} features diminishing and {110} planes expanding as etching is continued. AFM was used to image similar pits (see SI Figure 5). The inclination of the smooth sidewalls was measured from these images to be $-45 \pm 3°$ with respect to the {100} plane, confirming that they are {110} planes.

We also used electron beam lithography to fabricate circular silica disks to act as electron blocking masks during EBIE. Under highly anisotropic etch conditions, we obtain a faceted pillar with a very smooth surface. An example is shown in Figure 7j,k. Note the inset showing a top-down view of the pillar. The faceted pillar top can be seen through the circular outline of the silica mask, highlighting how the pillar geometry is determined by both the anisotropic etch kinetics and the mask geometry. Using isotropic etch conditions, we obtain cylindrical pillars (Figure 7l) with more undercutting of the silica etch mask.

These demonstrations illustrate the potential of EBIE for deterministic top-down nanofabrication in single-crystal diamond. Using isotropic EBIE it is possible to etch structures with arbitrary geometries at a maximized rate (see SI Figure 4). Conversely, anisotropic EBIE can be utilized to obtain large and smooth {110} planes that could be exploited for the fabrication of structures such as pyramids and V-grooves in {100} plane diamond.

CONCLUSIONS

We performed a detailed study of the EBIE kinetics of diamond and delineated the roles of oxygen and hydrogen species. We found that EBIE of single crystal diamond results in isotropic etching using O_2 as the precursor gas under anhydrous conditions and that the most likely etch reaction product leaving the diamond surface is CO. Addition of H_2 to the O_2 precursor gas selectively inhibits the etch rate of different crystal planes and makes etching anisotropic. The anisotropy gives rise to the formation of topographic surface patterns with symmetries defined by that of the crystal lattice and is attributed to preferential coverage of specific crystal planes by hydrogen. The coverage variations are a consequence of competitive adsorption of O and H and large differences in the adsorption energy of O on different crystal planes. The reduction in the etch rate caused by hydrogen is attributed to weakening of C–C surface bonds by O adsorbates and stabilization of the bonds by H. Our results constitute the first detailed description of anisotropic EBIE rate kinetics. In practice, the anisotropy can be controlled by varying the O_2 to H_2 partial pressure ratio and by radicalizing the precursor gas using a remote RF plasma generator. More broadly, the remote plasma can also be used to suppress undesired effects of residual H_2O molecules and to activate chemically stable gases and enable their use as precursors for electron stimulated surface processing. Isotropic EBIE with pure O_2 is capable of high-rate localized etching of diamond with nanostructure geometry dictated only by the electron beam scan pattern and/or mask used. Anisotropic EBIE using a H_2/O_2 mix can be used

to fabricate structures with large and smooth {110} crystal planes in single crystal diamond.

METHODS

Sample Preparation. The samples used in this study were boron-doped {100} plane, CVD grown, type 2a, single crystal diamonds, polished on both sides and purchased from Microwave Enterprises, Ltd. Extensive cleaning was found to be necessary for reproducibility and was performed prior to all experiments. Sequential ultrasonication in acetone, IPA, hexane, chloroform, ethanol, and ultrapure deionized water was first performed for 30 min each. Immersion in boiling piranha solution (3:1 mixture of 96% H_2SO_4:30% H_2O_2) at 155 °C with periodic replenishment of H_2O_2 was then performed for 30 min. This was followed by rinsing with DI water, a second piranha solution immersion with ultrasonication at room temperature, ultrasonication with ultrapure water, and finally drying in a stream of N_2. Samples were immediately loaded into the SEM chamber after cleaning and subject to overnight plasma cleaning with oxygen gas using a low-power remote plasma decontaminator system (EVACTRON model C from XEI scientific). The O_2 plasma cleaning further removes carbonaceous contaminants and lowers residual water concentration.

Electron Beam-Induced Etching of SC Diamond. EBIE was performed using a customized FEI Sirion field emission gun SEM, outfitted for variable-pressure operation. A homemade gas delivery system enables precursor input with high-precision flow control. Precursors used were high-purity hydrogen, oxygen, nitrogen, and Ar (all ≥99.99), obtained from Sigma-Aldrich as well as ultrapure deionized water. Gas input lines pass through a cold trap, held at 116 K for precursors other than H_2O. All gas lines were extensively flushed with dry N_2 prior to experiments.

Unless noted otherwise, all EBIE experiments, apart from those shown in Figure 7, were performed at room temperature using a 1.5 keV, 9.5 nA electron beam, scanned in a raster pattern to expose a 2.9 × 2.0 μm region of the sample surface to an average electron flux of 1.5×10^{10} e$^-$ μm^{-2} s^{-1}. The raster consisted of 484 lines per frame, 30 nm pitch between lines, and 1.68 ms linetime. An analog sine wave voltage signal was connected to the horizontal scan coil ('x-direction') and was therefore not discretized to individual dwell points. Each irradiation was performed for 20 min except the pits shown in Figure 4c–e,g,h, which were etched for 40 min. A pressure of approximately 9 Pa was used for all EBIE experiments utilizing a single precursor. For the experiments involving H_2 and O_2 mixing, the total chamber pressure was 9 ± 1.5 Pa. The pit shown in Figure 2g was an exception, and a total pressure of 12.6 Pa was used. The same remote plasma unit used for chamber decontamination (EVACTRON model C) was active during EBIE for all etch pits shown in Figure 2 and others where specified. An RF power of 5 W at 13.56 MHz was used for all plasma active experiments, chamber cleaning, and residual water suppression.

In Figure 7a, the inverse pyramid shown formed during EBIE of a 6.0 × 4.14 μm region with the same beam parameters described above and a H_2:O_2 ratio of 0.78. In Figure 7, approximately circular holes were etched with a 3 keV, 0.17 nA, stationary focused beam, and a 40 s total dwell time. Anisotropic EBIE was performed with a 1.5 keV beam scanned in a digitized raster pattern consisting of a square matrix of 10^6 pixels with 10 μs pixel dwell time. The etch frames and beam currents used were 18.5 × 18.5 μm, 21 nA for the array (Figure 7c–f), and 3.5 × 3.5 μm, 5.6 nA for individual etches (Figure 7g–i), resulting in electron fluxes of 3.81×10^8 and 2.85×10^9 e$^-$ μm^{-2} s^{-1}, respectively. A H_2:O_2 ratio of 0 and 2.2 with 10 Pa total chamber pressure was used for isotropic and anisotropic EBIE steps, respectively. Plasma was active during all steps. Silica disks of ~200 nm thickness were deposited by electron beam lithography using the negative resist hydrogen silsesquioxane (HSQ). EBIE of pillars was then performed using a 1.5 keV, 21 nA beam with the same raster pattern used for the pits of Figure 2, to expose a 4 × 2.7 μm region with the disk centered in the frame. Etch times were 4 and 1 h for the pillars shown in (j–k) and (l), respectively.

DFT Computational Method. The calculations presented in this work were performed using a DFT approach, within the generalized

gradient approximation (GGA) using the Perdew–Burke–Ernzerhof (PBE) functional for the exchange–correlation term.[58] We use periodic boundary conditions and localized atomic orbital basis set as implemented in SIESTA code, where the core–valence interaction is described by the norm conserving pseudopotential.[59,60] Double-ζ plus polarization orbitals (DZP) were applied, and the cutoff energy for the valence electrons was set to 750 Ry.[60,61] Γ point calculations have been used for a (6×6), (6×4), and (4×4) expansion of the {111}, {110}, and reconstructed {100} surfaces, consisting of 12 atomic layers, with a vacuum gap of *ca.* 25 Å. Full geometry optimization has been carried out for each system, and the convergence criteria for the energy and forces are 10^{-4} eV and 10^{-2} eV/Å, respectively.

ASSOCIATED CONTENT

ⓈSupporting Information

The Supporting Information is available free of charge on the ACS Publications website at DOI: 10.1021/acsnano.8b00354.

> Data and discussion concerning EBIE at elevated temperature, electron flux dependency, control experiments with inert gases as well as AFM and quantitative etch rate data is included. There are also further DFT calculations including bond lengths, surface formation energies, E_a and E_d for species other than O and H, and schematics illustrating adsorption geometries (PDF)

AUTHOR INFORMATION

Corresponding Author
*E-mail: James.Bishop@student.uts.edu.au.
ORCID Ⓘ
James Bishop: 0000-0001-6895-7544
Igor Aharonovich: 0000-0003-4304-3935
Milos Toth: 0000-0003-1564-4899

Author Contributions
§These authors contributed equally to this work.

Notes
The authors declare no competing financial interest.

ACKNOWLEDGMENTS

REFERENCES

(1) Sipahigil, A.; Evans, R. E.; Sukachev, D. D.; Burek, M. J.; Borregaard, J.; Bhaskar, M. K.; Nguyen, C. T.; Pacheco, J. L.; Atikian, H. A.; Meuwly, C.; et al. An Integrated Diamond Nanophotonics Platform for Quantum-Optical Networks. *Science* **2016**, *354*, 847–850.

(2) Greentree, A. D.; Fairchild, B. A.; Hossain, F. M.; Prawer, S. Diamond Integrated Quantum Photonics. *Mater. Today* **2008**, *11*, 22–31.

(3) Aharonovich, I.; Greentree, A. D.; Prawer, S. Diamond Photonics. *Nat. Photonics* **2011**, *5*, 397–405.

(4) Hausmann, B. J. M.; Bulu, I.; Venkataraman, V.; Deotare, P.; Lončar, M. Diamond Nonlinear Photonics. *Nat. Photonics* **2014**, *8*, 369–374.

(5) Mildren, R. P.; Butler, J. E.; Rabeau, J. R. CVD-Diamond External Cavity Raman Laser at 573 nm. *Opt. Express* **2008**, *16*, 18950–18955.

(6) Rath, P.; Ummethala, S.; Nebel, C.; Pernice, W. H. Diamond as a Material for Monolithically Integrated Optical and Optomechanical Devices. *Phys. Status Solidi A* **2015**, *212*, 2385–2399.

(7) Mortet, V.; Williams, O. A.; Haenen, K. Diamond: a Material for Acoustic Devices. *Phys. Status Solidi A* **2008**, *205*, 1009–1020.

(8) Macpherson, J. V. A Practical Guide to Using Boron Doped Diamond in Electrochemical Eesearch. *Phys. Chem. Chem. Phys.* **2015**, *17*, 2935–2949.

(9) Wort, C. J.; Balmer, R. S. Diamond as an Electronic Material. *Mater. Today* **2008**, *11*, 22–28.

(10) Balmer, R. S.; Brandon, J. R.; Clewes, S. L.; Dhillon, H. K.; Dodson, J. M.; Friel, I.; Inglis, P. N.; Madgwick, T. D.; Markham, M. L.; Mollart, T. P.; et al. Chemical Vapour Deposition Synthetic Diamond: Materials, Technology and Applications. *J. Phys.: Condens. Matter* **2009**, *21*, 364221.

(11) Matsumoto, T.; Kato, H.; Oyama, K.; Makino, T.; Ogura, M.; Takeuchi, D.; Inokuma, T.; Tokuda, N.; Yamasaki, S. Inversion Channel Diamond Metal-Oxide-Semiconductor Field-Effect Transistor With Normally Off Characteristics. *Sci. Rep.* **2016**, *6*, 31585 DOI: 10.1038/srep31585.

(12) Leech, P. W.; Reeves, G. K.; Holland, A. Reactive Ion Etching of Diamond in CF4, O2, O2 and Ar-Based Mixtures. *J. Mater. Sci.* **2001**, *36*, 3453–3459.

(13) Ando, Y.; Nishibayashi, Y.; Sawabe, A. 'Nano-rods' of Single Crystalline diamond. *Diamond Relat. Mater.* **2004**, *13*, 633–637.

(14) Smirnov, W.; Hees, J. J.; Brink, D.; Müller Sebert, W.; Kriele, A.; Williams, O. A.; Nebel, C. E. Anisotropic Etching of Diamond by Molten Ni Particles. *Appl. Phys. Lett.* **2010**, *97*, 073117–073113.

(15) Lehmann, A.; Bradac, C.; Mildren, R. P. Two-Photon Polarization-Selective Etching of Emergent Nano-structures on Diamond Surfaces. *Nat. Commun.* **2014**, *5*, 3341.

(16) Mildren, R. P.; Downes, J. E.; Brown, J. D.; Johnston, B. F.; Granados, E.; Spence, D. J.; Lehmann, A.; Weston, L.; Bramble, A. Characteristics of 2-photon Ultraviolet Laser Etching of Diamond. *Opt. Mater. Express* **2011**, *1*, 576–585.

(17) Specht, C. G.; Williams, O. A.; Jackman, R. B.; Schoepfer, R. Ordered Growth of Neurons on Diamond. *Biomaterials* **2004**, *25*, 4073–4078.

(18) Aharonovich, I.; Neu, E. Diamond Nanophotonics. *Adv. Opt. Mater.* **2014**, *2*, 911–928.

(19) Martin, A. A.; Toth, M.; Aharonovich, I. Subtractive 3D Printing of Optically Active Diamond Structures. *Sci. Rep.* **2015**, *4*, 5022.

(20) Fukui, T.; Doi, Y.; Miyazaki, T.; Miyamoto, Y.; Kato, H.; Matsumoto, T.; Makino, T.; Yamasaki, S.; Morimoto, R.; Tokuda, N.; et al. Perfect Selective Alignment of Nitrogen-Vacancy Centers in Diamond. *Appl. Phys. Express* **2014**, *7*, 055201.

(21) Zhu, D.; Zhang, L.; Ruther, R. E.; Hamers, R. J. Photo-Illuminated Diamond as a Solid-State Source of Solvated Electrons in Water for Nitrogen Reduction. *Nat. Mater.* **2013**, *12*, 836–841.

(22) Patten, H. V.; Meadows, K. E.; Hutton, L. A.; Iacobini, J. G.; Battistel, D.; McKelvey, K.; Colburn, A. W.; Newton, M. E.; Macpherson, J. V.; Unwin, P. R. Electrochemical Mapping Reveals Direct Correlation between Heterogeneous Electron-Transfer Kinetics and Local Density of States in Diamond Electrodes. *Angew. Chem., Int. Ed.* **2012**, *51*, 7002–7006.

(23) Utke, I.; Moshkalev, S.; Russell, P. *Nanofabrication using Focused Ion and Electron Beams: Principles and Applications*; Oxford University Press: Oxford, 2012.

(24) Randolph, S.; Toth, M.; Cullen, J.; Chandler, C.; Lobo, C. Kinetics of Gas Mediated Electron Beam Induced Etching. *Appl. Phys. Lett.* **2011**, *99*, 213103.

(25) Toth, M. Advances in Gas-mediated Electron Beam-Induced Etching and Related Material Processing Techniques. *Appl. Phys. A: Mater. Sci. Process.* **2014**, *117*, 1623–1629.

(26) Fu, J.; Wang, F.; Zhu, T.; Wang, W.; Liu, Z.; Li, F.; Liu, Z.; Denu, G. A.; Zhang, J.; Wang, H.-X. Single Crystal Diamond Cantilever for Micro-Electromechanical Systems. *Diamond Relat. Mater.* **2017**, *73*, 267–272.

(27) Randolph, S. J.; Fowlkes, J. D.; Rack, P. D. Focused, Nanoscale Electron-Beam-Induced Deposition and Etching. *Crit. Rev. Solid State Mater. Sci.* **2006**, *31*, 55−89.

(28) Randolph, S. J.; Fowlkes, J. D.; Rack, P. D. Focused Electron-Beam-Induced Etching of Silicon Dioxide. *J. Appl. Phys.* **2005**, *98*, 034902.

(29) Martin, A. A.; Toth, M. Cryogenic Electron Beam Induced Chemical Etching. *ACS Appl. Mater. Interfaces* **2014**, *6*, 18457−18460.

(30) Elbadawi, C.; Tran, T. T.; Kolíbal, M.; Šikola, T.; Scott, J.; Cai, Q.; Li, L. H.; Taniguchi, T.; Watanabe, K.; Toth, M.; Aharonovich, I.; Lobo, C. Electron Beam Directed Etching of Hexagonal Boron Nitride. *Nanoscale* **2016**, *8*, 16182−16186.

(31) Toth, M.; Lobo, C. J.; Knowles, W. R.; Phillips, M. R.; Postek, M. T.; Vladar, A. E. Nanostructure Fabrication by Ultra-high-resolution Environmental Scanning Electron Microscopy. *Nano Lett.* **2007**, *7*, 525−530.

(32) Utke, I.; Hoffmann, P.; Melngailis, J. Gas-assisted Focused Electron Beam and Ion Beam Processing and Fabrication. *J. Vac. Sci. Technol., B: Microelectron. Nanometer Struct.-Process., Meas., Phenom.* **2008**, *26*, 1197−1276.

(33) Lassiter, M. G.; Liang, T.; Rack, P. D. Inhibiting Spontaneous Etching of Nanoscale Electron Beam Induced Etching Features: Solutions for Nanoscale Repair of Extreme Ultraviolet Lithography Masks. *J. Vac. Sci. Technol., B: Microelectron. Nanometer Struct.-Process., Meas., Phenom.* **2008**, *26*, 963−967.

(34) Lassiter, M. G.; Rack, P. D. Nanoscale Electron Beam Induced Etching: a Continuum Model that Correlates the Etch Profile to the Experimental Parameters. *Nanotechnology* **2008**, *19*, 455306.

(35) Ganczarczyk, A.; Geller, M.; Lorke, A. XeF2 Gas-Assisted Focused-Electron-Beam-Induced Etching of GaAs with 30 nm Resolution. *Nanotechnology* **2011**, *22*, 045301.

(36) Martin, A. A.; Bahm, A.; Bishop, J.; Aharonovich, I.; Toth, M. Dynamic Pattern Formation in Electron-Beam-Induced Etching. *Phys. Rev. Lett.* **2015**, *115*, 255501−255505.

(37) Martin, A. A.; McCredie, G.; Toth, M. Electron Beam Induced Etching of Carbon. *Appl. Phys. Lett.* **2015**, *107*, 041603−041605.

(38) Caswell, H. L. Analysis of the Residual Gases in Several Types of High-Vacuum Evaporators. *IBM J. Res. Dev.* **1960**, *4*, 130−142.

(39) Lichtman, D. Adsorption-Desorption of Residual Gases in High Vacuum. *J. Vac. Sci. Technol.* **1965**, *2*, 70−74.

(40) Gleason, M. M.; Morgan, C. G.; Vane, R. Using a Thickness Monitor to Measure Contaminant Removal by Evactron Cleaning as a Function of Operating Parameters. *Microsc. Microanal.* **2007**, *13*, 1734.

(41) Isabell, T. C.; Fischione, P. E.; O'Keefe, C.; Guruz, M. U.; Dravid, V. P. Plasma Cleaning and its Applications for Electron Microscopy. *Microsc. Microanal.* **1999**, *5*, 126−135.

(42) Niitsuma, J.-i.; Yuan, X.-l.; Koizumi, S.; Sekiguchi, T. Nanoprocessing of Diamond Using a Variable Pressure Scanning Electron Microscope. *Jpn. J. Appl. Phys.* **2006**, *45*, L71.

(43) Fox, D.; O'Neill, A.; Zhou, D.; Boese, M.; Coleman, J. N.; Zhang, H. Z. Nitrogen Assisted Etching of Graphene Layers in a Scanning Electron Microscope. *Appl. Phys. Lett.* **2011**, *98*, 243117.

(44) Hesketh, P. J.; Ju, C.; Gowda, S.; Zanoria, E.; Danyluk, S. Surface Free Energy Model of Silicon Anisotropic Etching. *J. Electrochem. Soc.* **1993**, *140*, 1080−1085.

(45) Elwenspoek, M. On the Mechanism of Anisotropic Etching of Silicon. *J. Electrochem. Soc.* **1993**, *140*, 2075−2080.

(46) Bean, K. E. Anisotropic Etching of Silicon. *IEEE Trans. Electron Devices* **1978**, *25*, 1185−1193.

(47) Petrini, D.; Larsson, K. A Theoretical Study of the Energetic Stability and Geometry of Hydrogen-and Oxygen-terminated Diamond (100) Surfaces. *J. Phys. Chem. C* **2007**, *111*, 795−801.

(48) Zhao, S.; Larsson, K. Theoretical Study of the Energetic Stability and Geometry of Terminated and B-doped Diamond (111) Surfaces. *J. Phys. Chem. C* **2014**, *118*, 1944−1957.

(49) Derry, T. E.; Makau, N. W.; Stampfl, C. Oxygen Adsorption on the (1×1) and (2×1) Reconstructed C (111) surfaces: A Density Functional Theory Study. *J. Phys.: Condens. Matter* **2010**, *22*, 265007.

(50) Stampfl, C.; Derry, T. E.; Makau, N. W. Interaction of Diamond (111)-(1×1) and (2×1) Surfaces with OH: A First Principles Study. *J. Phys.: Condens. Matter* **2010**, *22*, 475005.

(51) Kern, G.; Hafner, J. Ab Initio Calculations of the Atomic and Electronic Structure of Clean and Hydrogenated Diamond (110) Surfaces. *Phys. Rev. B: Condens. Matter Mater. Phys.* **1997**, *56*, 4203.

(52) de Theije, F. K.; van der Laag, N. J.; Plomp, M.; Van Enckevort, W. A Surface Topographic Investigation of (001) Diamond Surfaces Etched in Oxygen. *Philos. Mag. A* **2000**, *80*, 725−745.

(53) Peaker, C. V.; Goss, J. P.; Briddon, P. R.; Horsfall, A. B.; Rayson, M. J. Di-nitrogen-vacancy-hydrogen Defects in Diamond: a Computational Study. *Phys. Status Solidi A* **2015**, *212*, 2616−2620.

(54) Moustafa, S.; Tokuda, N.; Inokuma, T. Density Functional Studies of Surface Potentials for Hydrogen and Oxygen Atoms on Diamond (111) Surfaces. *Jpn. J. Appl. Phys.* **2014**, *53*, 02BD01.

(55) Loh, K. P.; Xie, X.; Yang, S.; Zheng, J. Oxygen Adsorption on (111)-Oriented Diamond: a Study with Ultraviolet Photoelectron Spectroscopy, Temperature-Programmed Desorption, and Periodic Density Functional Theory. *J. Phys. Chem. B* **2002**, *106*, 5230−5240.

(56) Tian, S.; Sun, W.; Hu, Z.; Quan, B.; Xia, X.; Li, Y.; Han, D.; Li, J.; Gu, C. Morphology Modulating the Wettability of a Diamond Film. *Langmuir* **2014**, *30*, 12647−12653.

(57) Escobar, J. V.; Garza, C.; Alonso, J. C.; Castillo, R. Super-Mercuryphobic and Hydrophobic Diamond Surfaces with Hierarchical Structures: Vanishment of the Contact Angle Hysteresis with Mercury. *Appl. Surf. Sci.* **2013**, *273*, 692−701.

(58) Perdew, J. P.; Burke, K.; Ernzerhof, M. Generalized Gradient Approximation Made Simple. *Phys. Rev. Lett.* **1996**, *77*, 3865.

(59) Blöchl, P. E. Projector Augmented-Wave Method. *Phys. Rev. B: Condens. Matter Mater. Phys.* **1994**, *50*, 17953.

(60) Hamann, D. R.; Schlüter, M.; Chiang, C. Norm-Conserving Pseudopotentials. *Phys. Rev. Lett.* **1979**, *43*, 1494.

(61) Blöchl, P. E.; Jepsen, O.; Andersen, O. K. Improved Tetrahedron Method for Brillouin-Zone Integrations. *Phys. Rev. B: Condens. Matter Mater. Phys.* **1994**, *49*, 16223.